Understanding Shape Memory Alloy Torsional Actuators: From the Conceptual to the Preliminary Design

actuators

MDPI

Article

Understanding Shape Memory Alloy Torsional Actuators: From the Conceptual to the Preliminary Design

Mario Sansone [1], Salvatore Ameduri [2], Antonio Concilio [2] and Enrico Cestino [1,*]

[1] Department of Mechanical and Aerospace Engineering, Politecnico di Torino, 10129 Turin, Italy; mario.sansone@studenti.polito.it
[2] Centro Italiano Ricerche Aerospaziali—CIRA, 81043 Capua, Italy; s.ameduri@cira.it (S.A.); a.concilio@cira.it (A.C.)
* Correspondence: enrico.cestino@polito.it

Abstract: Shape memory alloy actuators have been studied for more than thirty years. Many experimental tests have been performed, and several patents have been registered. However, designing such devices is still a challenging task. On the one hand, models are not yet able to provide the accuracy required to replace a substantial portion of the experimental tests; on the other hand, it seems that a gap exists in the literature between the main ideas behind SMA torsional actuators and their actual implementation. This work is a systematic effort to fill this gap, helping researchers and designers in developing SMA torsional actuators with a particular focus on aeronautical applications. This paper reports all the steps toward the preliminary design of such devices, using a state-of-the-art, commercially available FEM software. Moreover, the SMA rods' behaviour under mechanical and thermal loading is thoroughly examined, looking at monitoring stress, temperature, torque and martensite evolution simultaneously, and thus providing a holistic vision of the macroscopic phenomena involved during phase transformations. Simple aerodynamic load predictions are also performed, using Xfoil for three classes of aircraft (medium size UAV, Four-Seat Aircraft and Regional Transport Aircraft).

Keywords: shape memory alloy; torsional actuator; hinge moment; flap; adaptive trailing edge; UAV; Cessna 172; ATR 42; Xfoil; nastran

Citation: Sansone, M.; Ameduri, S.; Concilio, A.; Cestino, E. Understanding Shape Memory Alloy Torsional Actuators: From the Conceptual to the Preliminary Design. *Actuators* **2022**, *11*, 81. https://doi.org/10.3390/act11030081

Academic Editor: Kenji Uchino

Received: 26 January 2022
Accepted: 4 March 2022
Published: 6 March 2022

1. Introduction

Shape Memory Alloys are metals capable of undergoing large deformations (up to 10% and beyond) [1] as a consequence of lattice swap and crystallographic reorientation during a solid-state transformation. Moreover, SMAs can recover most of the residual-stress-induced deformation upon heating. This unique property makes them promising candidates as solid-state actuators. The main idea underlying the implementation of shape memory, alloy-based torsional actuators is fairly straightforward. Let us consider an SMA rod, or tube, clamped at one end and deformed under torque in such a way as to rotate its free edge up to a certain angle, enough to induce phase transformation (from an austenite to martensite phase). Heating the specimen to bring it over a so-called activation temperature, until the full-transformation temperature is reached (Austenite finish temperature, or A_f), will bring it back to its original undeformed shape, generating rotary actuation. The main advantage of such devices is a reduced part number, and lower maintenance issues, resulting in them becoming simpler, more efficient, and more reliable. Furthermore, they can be integrated into structures as further load-bearing elements, therefore reducing the added weight. Generally, SMA actuators may provide a way to morph wing technologies' industrial applications, since they allow distributed actuator arrays to be spread along the aerodynamic surfaces, with minimal impact in terms of volume occupation, general increases in cost, and weight penalties. An essential aspect concerns SMA energy density, which is over 1000 J/kg, [1].

Recently, many shape memory, alloy-based actuators have been developed and patented to improve the overall performance of movable surfaces. Among others, those presented by the Boeing Company, and particularly [2–5], may be considered as the most relevant examples. Mabe et al. [2] developed an SMA actuator for movable surfaces, including locking mechanisms and a clutch or spline coupling between the driver and the driven system. This device also includes a spring, which can work together with the locking mechanism to achieve a faster actuation. Arbogast et al. [3,4] NiTinol actuator is integrated into the rotor blade as a structural element, controlling the blade twist. The active part of the actuator is composed of two parallel SMA torque tubes that simultaneously activate during each actuation. Thus, by leveraging two-way SME, it is possible to overcome the necessity for a return spring, which is needed for configurations in which stress-assisted SME is required. Moreover, thermal electric modules and a thermosyphon are used to optimise temperature management. Calkins et al. [5] developed an Adaptive Trailing Edge (ATE) consisting of a little split-flap of 2% of the local chord, which can deflect in a range between 30 degrees up and 60 degrees down. The overall apparatus is redundant for safety reasons and includes secondary components that also provide a locking and damping function. A dual-tube design is adopted to control the flap motion from a martensite to austenite transformation for both deployment and retraction via heating. This device was tested in flight on a Boeing 737–800, leading to maturation from TRL4 to TRL7.

Other remarkable studies in the field were developed by NASA, inside the Spanwise Adaptive Wing (SAW) programme [6], and by the European Consortium of Universities and Research Centers, coordinated by the University of Bristol (Shape Adaptive Blades for Rotorcraft Efficiency, SABRE), whose results led to a patent application concerning an SMA actuation system to increase rotor blade efficiency [7]. The SAW programme was developed to articulate outboard wing sections using SMA torsional actuators. The project's aim is twofold: saving aeroplanes planform space for specific applications as aircraft carrier missions, and augmenting lateral–directional stability. While static actuation was performed on a full-scale F18 wing, flight tests were carried out on a UAV platform, denominated Area-I PTERA, in 2017. Furthermore, the patent proposal from [7] consists of a morphing system, based on an SMA solid torsional actuator that can alter the twist law of the blade to improve helicopter performance in specific flight regimes (hover and vertical flight), which are generally penalized by the conventional design, in favor of more extended phases of the flight envelope (cruise).

Speaking of SMA systems modelling, it can be stated that the reference works in the sector are represented by the works reported in [8,9]. Indeed, Auricchio et al. [8] developed a refined and general three-dimensional phenomenological constitutive model for shape memory alloys, accounting for a variety of physical phenomena, such as martensite reorientation and different kinetics between forward- and reverse-phase transformations, as well as smooth thermo-mechanical response, low-stress phase transformations, and transformation-dependent elastic properties. Moreover, Popov et al. [9] designed a 3D constitutive model for SMAs based on a modified phase-transformation diagram. This model considers both the direct conversion of austenite into detwinned martensite and the detwinning of twinned martensite, making it suitable to predict the behaviour of SMAs undergoing complex thermomechanical loading paths in a stress–temperature space.

If the behaviour of both rods and tubes under torque loading are referenced, a significant contribution to the literature may be found in [10,11]. In these latter cases, remarkable original models are proposed, based on the same 3D general constitutive law, developed from considerations related to the Gibbs free energy.

In the latest thirty years, many design approaches have been presented, and several mathematical models were developed in response to the increasing demand for accuracy in predicting SMA behavior. However, despite this effort, the design of such devices still has unsolved issues. This work presents a novel approach for designing torsional SMA-based devices, from the early concept to the preliminary layout definition. Moving from shape memory alloys' fundamental diagrams, an original interpretation of the actuator diagrams is introduced, and guidelines for implementing a specifically suited design strategy within

the commercial software are given. Patterns are introduced to estimate the SMA behaviour in operational conditions and to evaluate the impinging aerodynamic loads. In summary, the paper aims to provide a reference for conceiving shape-memory-alloy-based torsional actuators with a particular focus on their aeronautical applications; the proposed approach uses preferentially commercial off-the-shelf engineering solutions. A final discussion analyses both its potential and its current limitations.

2. Materials and Methods

2.1. Preliminary Remarks

2.1.1. Phase Diagram

Depending on the applied stress and temperature, SMA can exist in two different phases: austenite, exhibiting a high-symmetry crystal lattice, and martensite, with a low-symmetry monoclinic lattice. While austenite is associated with a unique macroscopic specimen shape, martensite exhibits different macroscopic shapes according to the amount and direction of the induced deformation strain (i.e., the deformation obtained from lattice swap and crystallographic reorientation). This mechanism is known as detwinning; indeed, reference is made to twinned and detwinned martensite for the states of 0% and 100% of the transformation strain associated with the specimen under examination.

The alloy considered in this work is NiTiNol due to its superior performance in terms of mechanical properties and strain recovery, which makes it preferable with respect to other SMAs for the examined application. Within this alloy's typology, a class with superelastic behavior at room temperature and characterized by stress transformation values below 350 MPa was selected. For typical stress/temperature gradients of 6–7 MPa/°C, the austenite start and finish temperatures remain in the range between −20 and 30 °C at zero stress. As a pre-load is applied, inducing a stress field within the SMA, such transformation temperatures arise well over the maximum operational temperature of a vehicle, typically 80 °C.

Phase diagrams, simplified in Figure 1c, show the existence of different phases, depending on temperature and stress, for a simple unidirectional loading test. Moreover, their great utility is to show the interdependence between transformation temperatures and stresses. Indeed, stress-induced phase and shape transformation begins and finishes at different values depending on temperature, and temperature-induced transformation, in the same way, is influenced by the applied stress.

2.1.2. Stress–Strain Diagram

For a given temperature, it is possible to load and unload an SMA under unidirectional stress, obtaining a hysteresis loop in the stress–strain diagram, as shown in Figure 1a. The corners of the parallelogram are, in order, the martensite start, martensite finish, austenite start and austenite finish stresses for the investigated temperature. This behaviour, known as the pseudoelastic effect, occurs because the considered temperature is sufficiently high to activate the strain recovery when the load expires. Changing the temperature will affect the values of the transformation stresses. The shape memory effect occurs in cases where the temperature is low enough that, upon unloading, the strain is not instantly recovered, but a heat source is required.

2.1.3. Strain–Temperature Diagram

A similar hysteresis loop can be represented in the Strain-Temperature field at a given stress, as illustrated in Figure 1b. In this case, the corners of the parallelogram represent the austenite start, austenite finish, martensite start and martensite finish temperature at a given stress. Again, different stress magnitudes correspond to different transformation temperatures values.

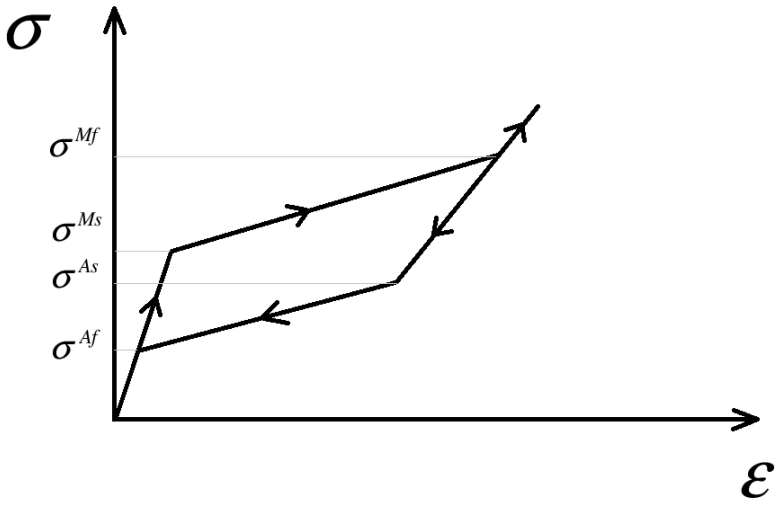

(**a**) Stress Strain diagram.

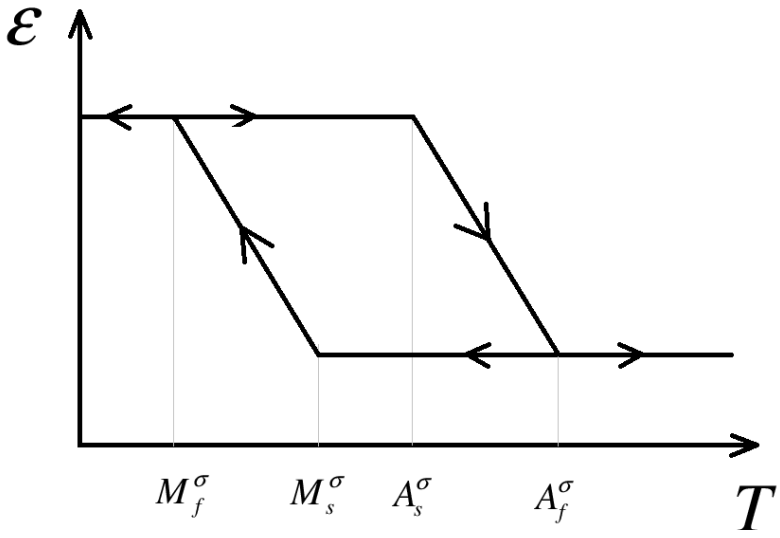

(**b**) Strain Temperature diagram.

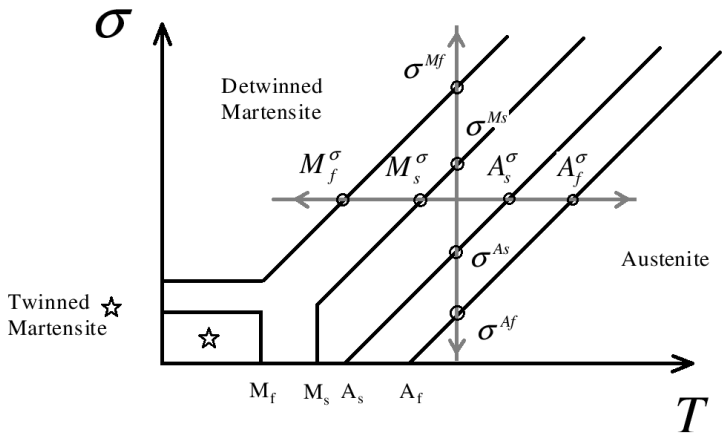

(**c**) Stress Temperature diagram.

Figure 1. Simplified representation of the fundamental diagrams.

2.2. Graphical Analysis

2.2.1. Theoretical Approach Based on Stiffness Curve Comparison

The three charts mentioned above can be manipulated and combined into what will be referred to hereafter as the actuator's diagram. First of all, it is interesting to note that the torque-angle characteristic of SMA tubes and rods shows a similar behaviour with respect to the stress–strain diagram under unidirectional loading. Similarly, the angle temperature response recalls that of the strain-temperature, again showing a hysteresis loop. It is important to underline that, in rods subjected to torque loading, the transition between austenite and martensite begins in the outer section of the component, where the stress is higher, and subsequently spreads toward the inside of the same, so the linear segments of the hysteresis loops should be replaced by smoother curves in both torque-angle and temperature-angle diagrams. Moreover, the stress in the inner core along the radius of the specimen will never be high enough to trigger the austenite-to-martensite transformation. As a result, for torque rods, the lines referred to in the 100% martensite phase actually represent an asymptote. Experimental data on the thermal and mechanical cycle of torque SMA torque tubes can be found in [12,13]. To provide a more intuitive representation of the phenomena under investigation, the diagrams illustrated below are represented as those referring to a unidirectional loading case. Moreover, because stress varies with the radius in a rod subjected to a torsional load, the applied torque will be reported instead of stress to avoid ambiguity. The actuator's diagram is built beginning from the torque-angle field.

The following approach consists of a series of steps in which classical torque-angle charts are manipulated to represent SMA actuators' behaviour more directly. Figure 2 represents the torque-angle characteristic (C and θ, respectively) for two different components in the same reference frame. In particular, the red and orange lines show a simplified SMA, exhibiting a pseudoelastic effect at temperature $T1$. In particular, red segments represent the loading path, while the orange ones represent the unloading path. The blue line, instead, shows a linear elastic response, such as that of a torsional spring. For the coupled deflection angles, $\theta 1$ and $\theta 2$, the reaction torque of the two components is equal and opposite, so that $C1 = C2$ in absolute value.

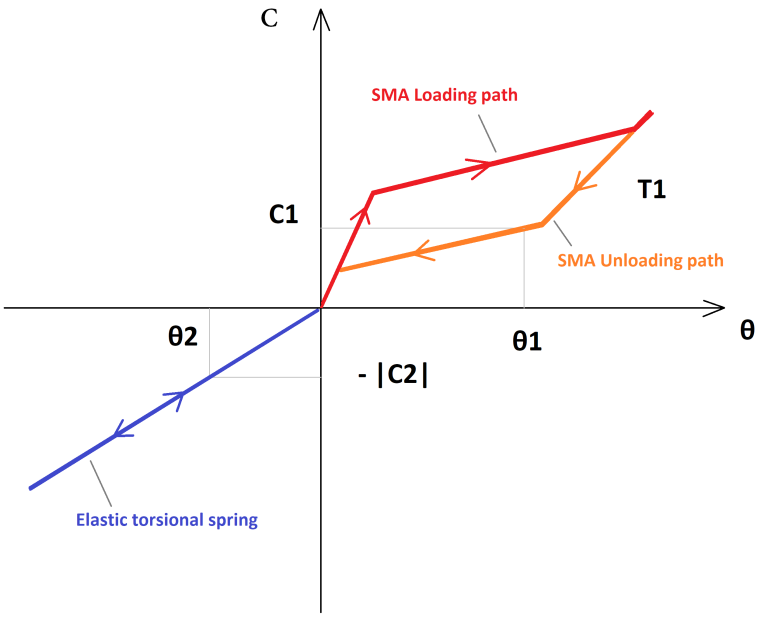

Figure 2. Actuator diagram—Step 1.

A graphical representation of these components is presented in Figure 3, in which, moreover, the torsional spring torque is substituted by its modulus. This representa-

tion aims to immediately obtain that the reaction torque of the components is equal in absolute values.

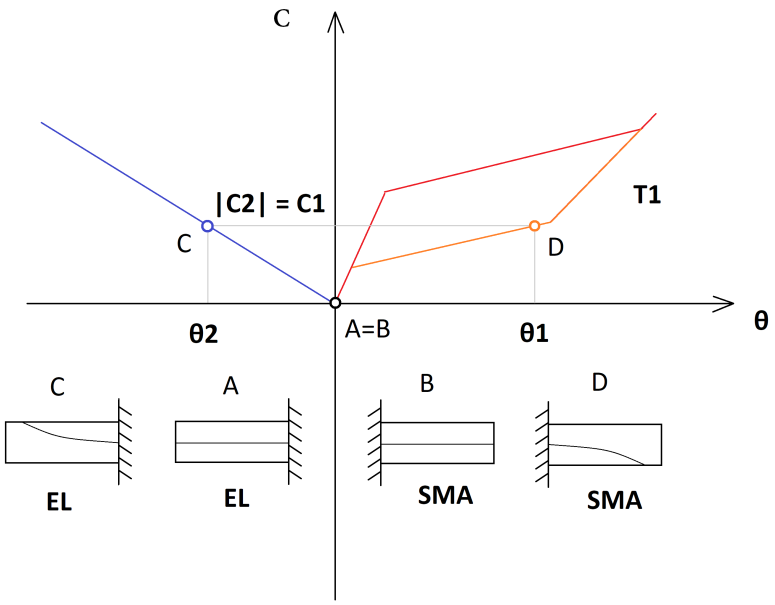

Figure 3. Actuator diagram—Step 2.

A more functional representation is achieved in Figure 4. Indeed, the origin of the θ axis related to the torsional spring is translated rightward, overlapping $\theta 1$ and $\theta 2$ in their respective reference frame. Despite having two θ–axis could appear less intuitive, the advantage of this representation method is that any change in the equilibrium position $\theta 1$, $\theta 2$ is immediately recognised for both the SMA and the linear elastic spring.

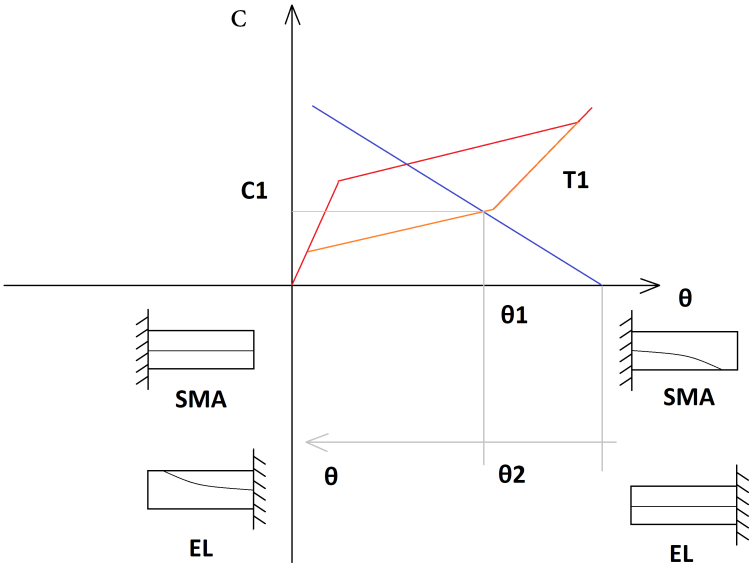

Figure 4. Actuator diagram—Step 3.

Indeed, as shown in Figure 5, the coupling of the two preloaded components constrains both of them to rotate on the same angle around the original equilibrium position, upon a perturbation. At this point, thermal-induced transformation comes into play. As temperature rises, a martensite to austenite transformation occurs. This leads to a modi-

fication in the torque-angle SMA characteristic that can be visualised as an upward and rightward translation of the hysteresis loop.

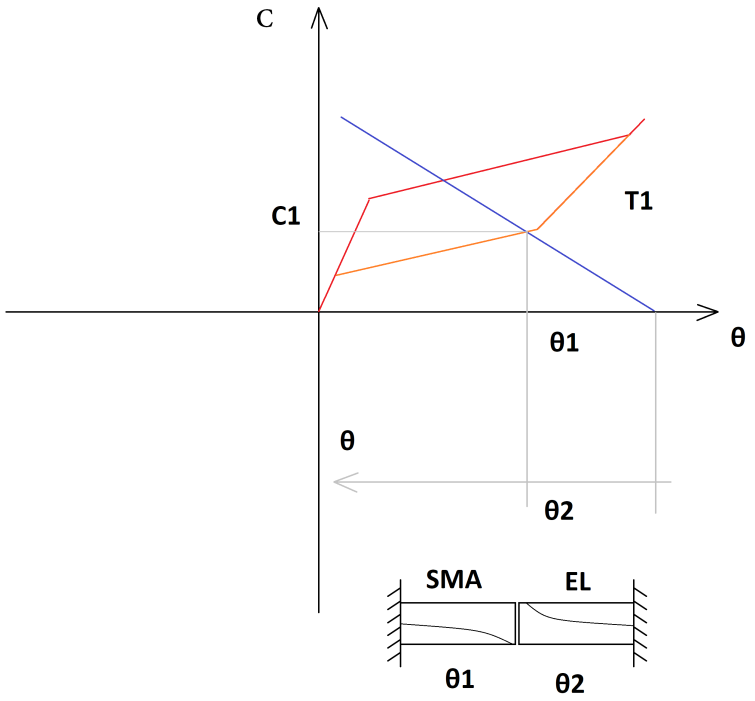

Figure 5. Actuator diagram—Step 4.

Consequently, at a given temperature $T2 > T1$, a new equilibrium point is established, as shown in Figure 6. The recovery of austenitic shape leads to an angular actuation of $\Delta\theta$ under a variable load. This representation immediately shows how the SMA component returns toward its undeformed configuration while the torsional spring increases its deformation (note that a rigorous representation of $\Delta\theta$ sign has been sacrificed for greater clarity). Consequently, during the forward actuation, the SMA is heating and unloading; meanwhile, in the reverse actuation, the SMA undergoes cooling and loading. This consideration is crucial to understand that, upon heating and shape recovery, the equilibrium point is obtained from the intersection of the load line with the unloading segment of the SMA loop ($M \rightarrow A$ segment), while, during cooling, the loading section ($A \rightarrow M$) has to be considered. It is clear at this point that aspects of both thermal-induced and stress-induced transformation are involved.

The aspects described above are further illustrated in [14], where SMA elements were used for the actuation of morphing trailing edges. The actuator design moved from the force equilibrium, and the displacements' congruence conditions, between the shape memory alloy and the driven structure. A graphical tool, overlapping SMA load–unload cycles and the equivalent structural elastic line, was used to describe the evolution of the working points of the morphing system vs. the temperature.

The angle-temperature chart and the torque-temperature diagram are included to monitor torque, rotation and temperature continuously with time. Note that, operating under high-stress and -temperature conditions, a simplified version of the stress-temperature diagram is reported.

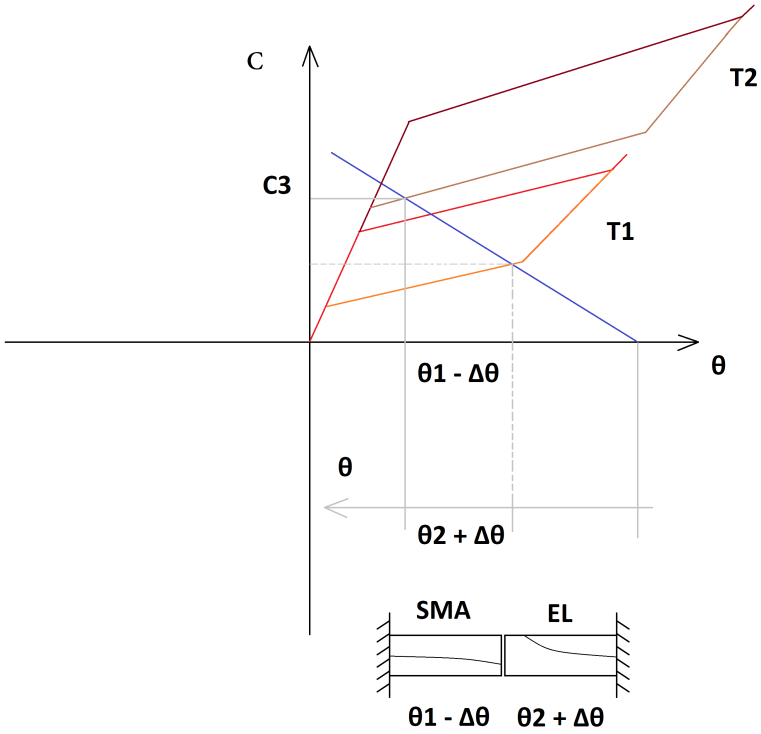

Figure 6. Actuator diagram—Step 5.

2.2.2. Actuator Architecture

The actuator architecture is a compromise between an overall simplicity of the system and the accomplishment of real-world loading conditions. Actual actuators usually employ two torque tubes, avoiding the use of a contrast spring and thus optimizing the system weight. Moreover, leveraging on the two-way shape memory effect, both tubes can provide torque in both direct and reverse motions. However, aiming to provide a general procedure, and to keep the general architecture as simple as possible, the architecture proposed here includes an SMA torque rod and a return torque spring, which are collinearly coupled. In this way, the forward actuation exploits direct transformation ($M \rightarrow A$), while the backward phase transformation is assisted by the applied contrast element force (stress-assisted, two-way memory effect). To achieve real-world loading conditions, a blocking mechanism is encluded that enables the SMA component to cool down once the desired position is reached. The principal advantage of this choice is the resulting energy savings; however, even with a simple upgrade, the results are not trivial. Examples of the utilisation of this kind of devices can be found in a flap or adaptive trailing edge. With the intention of keeping operations simple, the actuator is designed to only provide movement in the forward direction, while a further damped return spring system controls the backward motion. A similar solution was implemented in [2]. To deactivate the SMA tube while maintaining an unaltered control surface position, a spline coupling system or a clutch is required. These components are essential to decouple the driving SMA rod rotation from that of the driven shaft during cool-down. In this way, upon cooling, the SMA can recover the shape associated with its martensitic phase, while the driven shaft keyed with the control surface maintains its angular position thanks to the locking mechanism. Upon locking release, the driven shaft recovers its original position. In the case of an adaptive trailing edge, in which upward deflection is also needed, the equilibrium position of the return mechanism can be set with a certain offset with respect to the hinge zero angular displacement, so that the actuator can provide either negative or positive deflections, despite always operating in the same direction. A spline assembly similar to that presented in [2] and its working scheme is illustrated in Figure 7. Two different configurations are examined, considering an architecture with and without a clutch, to decouple the driving

shaft from the driven one. Figure 8 shows a schematic image of the architecture described above.

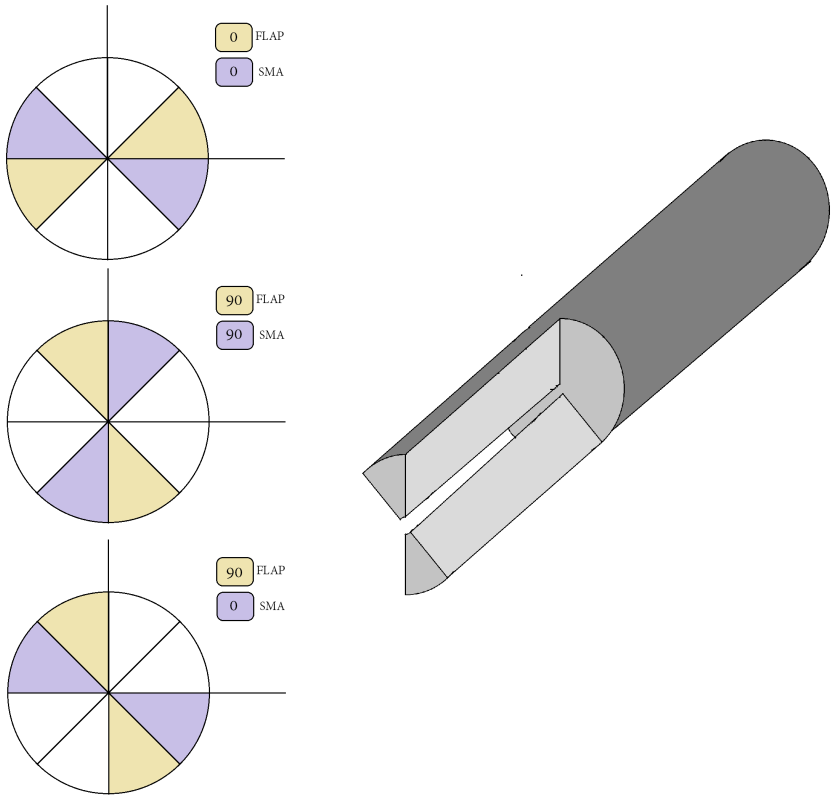

Figure 7. Spline coupling working principle.

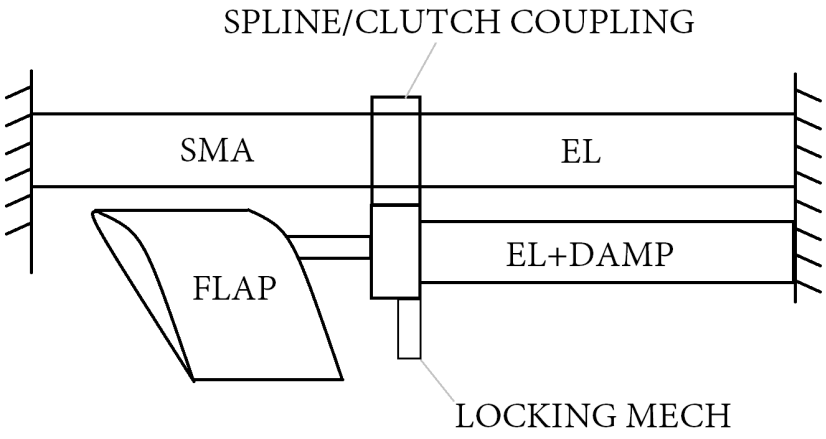

Figure 8. Outline of the SMA actuator under investigation.

2.2.3. Actuator with Clutch

At this point, it is possible to examine the working scheme and the expected response of the SMA rod during actuation. All the steps are enumerated coherently in Figures 9 and 10, which represent a simplified schematic of the actuator. Note that the numbers presented on the top of each box represent a hypothetical angle of deflection for the related assembly, while the red and green dots represent an activated or de-activated

locking mechanism, respectively. Moreover, a continuous rectangle between the "SMA+EL box" and the rest of the system represents a disengaged clutch (the systems are coupled); meanwhile, a discontinuity between the two of them represent that the clutch is engaged (the systems are decoupled). Point 1 represents the initial equilibrium condition between the SMA rod and the driven system, represented by the green line. Upon heating, before reaching A_s^σ (which indicates the temperature intercepted on the A_s line for a given stress σ. This kind of notation will often be reported hereafter); no significant changes can be appreciated on the stress–strain diagram (Point 2). Further temperature increases, beyond A_s^σ induce the martensite-to-austenite transformation, resulting in the original shape recovery. Consequently, from point 2 to 3, the SMA rod angle and strain decrease following the load line equilibrium condition. This means that the 2 $\rightarrow$ 3 transformation induced by temperature rise undergoes a variable load. The yellow shaded lines in stress-temperature and strain-temperature diagrams are hypothetical paths based on the expected starting and finishing equilibrium points. Note that point 3 also represents the SMA rod's angular position at the end of the forward actuation. At this step, the locking system is activated to hold the flap in position, and the clutch is engaged, enabling the SMA rod to cool down and return to its martensitic phase. As the driver and driven systems are decoupled, the overall torque applied to the SMA drops down to the horizontal load line, as shown in points 3 and 4. Simultaneously monitoring all three charts, it is evident that temperatures remain constant, and stress decreases as well as strain, following the high-temperature SMA characteristic. Again, the 3 $\rightarrow$ 4 loading path on stress–strain and strain-temperature diagrams are based on starting and finishing equilibrium points. Cooling the SMA rod down to M_s^σ does not involve any macroscopic stress–strain change, as shown in points 4 and 5. Further decreases in temperature trigger the stress-assisted shape memory effect. The transformation ends on Point 6 as M_f^σ is reached. Strictly speaking, cooling down the SMA from point 6 to 7 under constant torque should induce a further increase in the rod strain, moving to the 100% martensite characteristic. Still, to simplify this dissertation, it can be assumed that Points 1 and 7 are sufficiently close to M_f^σ so that no macroscopical effects can be observed.

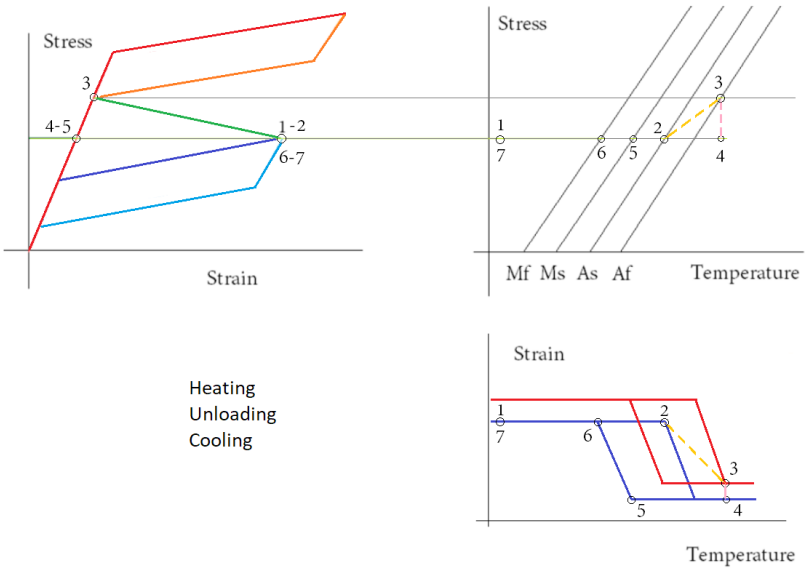

Figure 9. Graphical analysis—Actuator with clutch.

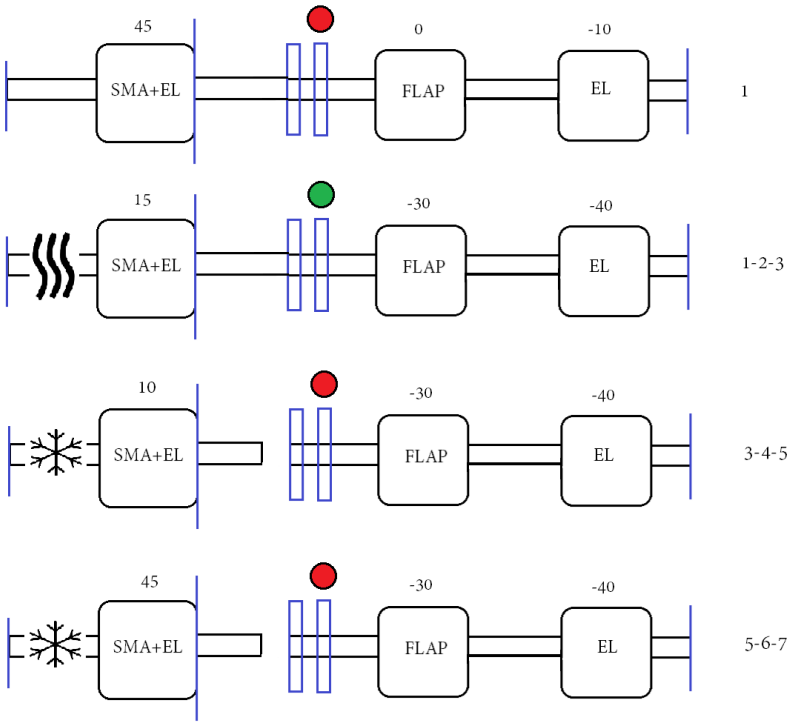

Figure 10. Functioning scheme—Actuator with clutch.

2.2.4. Actuator without Clutch

The working scheme and the graphical analysis of the actuator without clutch are reported in Figures 11 and 12. Most of the transformations involved in an actuator without a clutch are the same as illustrated in the previous section. Indeed, nothing changes up to Point 3. The spline coupling allows to decouple the SMA rod backward motion from that of the driven system, however, the forward motion still remains constrained. Differently from the case presented above, upon cooling the SMA rod cannot undergo strain decreasing since the lower angular position is imposed by the flap position. Consequently, as A_s^{σ} for the point 3 stress level is reached, $A \rightarrow M$ transformation begins but no strain changes can occur, since the returning force at this step is not high enough. Further temperature drop increases the martensitic volume fraction, lowering the component stiffness. As a result, stress must decrease, while strain remains constant during the 4 to 5 transformation. At step 5, the returning force is sufficient to trigger the stress-assisted two-way memory effect, so that the original shape is recovered at point 6. The following steps are not different with respect to the clutch provided actuator. In the light of this working sequence, a big concern emerges. During the transformation $4 \rightarrow 5$ according to established literature, austenite to twinned martensite transformation cannot occur in a high-stress, high-temperature region of the phase diagram as in this case. On the other hand, $4 \rightarrow 5$ transformations don't involve any macroscopic shape recovery, thus suggesting that detwinned martensite, which is associated with macroscopic shape deformation, is not forming. Consequently, two possibilities can be found:

- The $4 \rightarrow 5$ transformation generates twinned martensite, eventually decaying the SMA actuator performance due to retained martensite and the consequent decrease in of transformation strain over time. On the other hand, this would open a new region in the phase diagram, that has not been considered before.
- The $4 \rightarrow 5$ transformation generates detwinned martensite, even without a macroscopic shape change, thus preserving the transformation strain and the SMA performance over time.

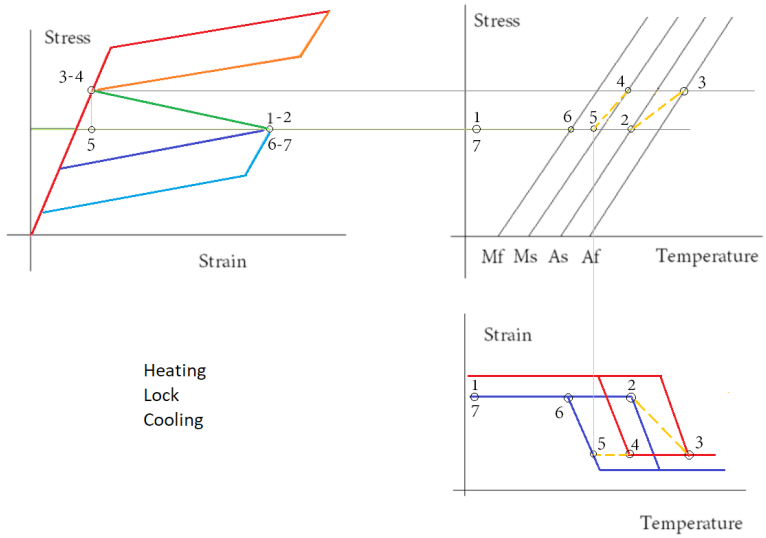

Figure 11. Graphical analysis—Actuator without clutch.

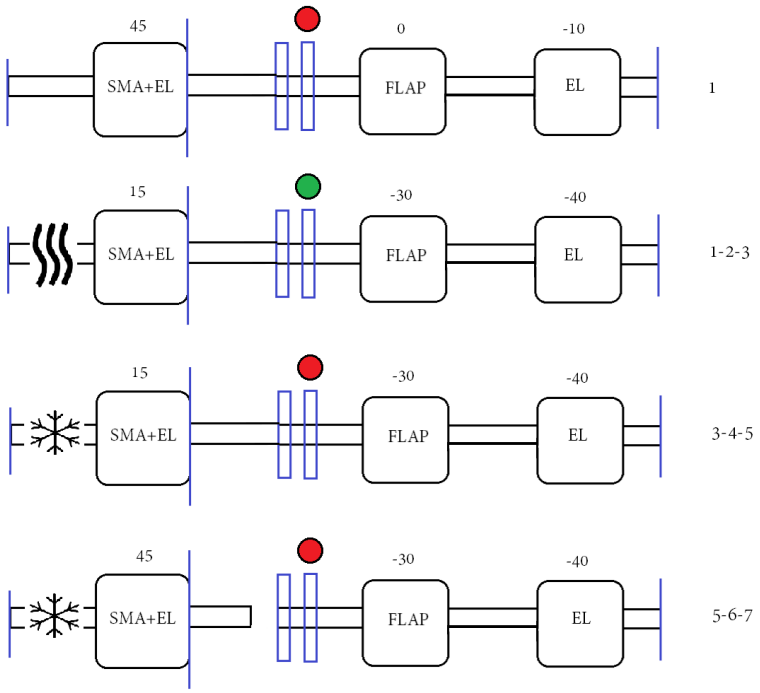

Figure 12. Functioning scheme—Actuator without clutch.

In this context, Popov and Lagoudas [9] examined a similar situation, obtaining the response predicted by their model, considering, for simplicity, a rod in a uniaxial stress state. Under high-stress and -temperature conditions with 100% austenite phase, the specimen is constrained and then gradually cooled. They observed that the transformation strain has a maximum value that is an order of magnitude greater than the elastic strain (which is fixed during the cooling). As a result, just a small amount of phase transformation is necessary to produce transformation strains that are comparable to the elastic strain, resulting in a significant reduction in stress. In view of this, the second possibility appears to be more realistic; however, it is worth mentioning that the results presented above are not experimental data, but model-predicted. Moreover, it would be a good measure to perform an experimental test on long-term response to dispel any remaining doubt.

2.3. FEM Validation

2.3.1. FEM Model and Material Validation

The conceptual design based on the graphical analysis was validated, creating original models using MSC Patran and Nastran (v2017.1), which adopts Auricchio's formulation [15,16]. Specific criteria drove their realization. These include the non-linearity of the elements, to support the constitutive law of the SMA, and the number of elements along the radius, to adequately describe the stress–strain–martensite phase behaviour within the cross-section.

The shape memory alloys were defined using MATSMA material property [17], originally designated for MSC Marc and compatible with Nastran SOL400 (implicit non-linear static solution). The NiTi alloy material parameters for the model under examination were extrapolated from Taheri et al. [11] and summarized in Table 1.

Table 1. MATSMA entries (N, mm, ton).

1	2	3	4	5	6	7	8	9	10
MATSMA	MID	MODEL	T_0	L					
	E_a	ν_a			ρ_a	σ_s^{AS}	σ_f^{AS}	C_a	
	E_m	ν_m			ρ_m	σ_s^{SA}	σ_f^{SA}	C_m	
MATSMA	1	1	24	0.023					
	25×10^3	0.330			6.5×10^{-9}	150	325	6.8	
	15×10^3	0.330			6.5×10^{-9}	175	45	7.6	

For the specimen discretisation, solid elements CHEXA-20 and CPENTA-15 were adopted, which are modified isoparametric elements that use selective integration points for different strain components [18]. Moreover, to achieve simple outputs, two RBE2 spider elements were connected at either end to apply loads and constraints. The subject of the finite-element analysis is an SMA rod, 200 mm long and with a radius of 5 mm, whose expected performance is compatible with a UAV flap actuator device, as shown later in this article. Despite a tube offering higher torque outputs for the same weight, rods are less susceptible to buckling effects; moreover, this work aims to discover the SMA behaviour in the inner radial parts, as the generated lower stress should lead to partial transformations. To validate the model, the FEM results under uniaxial loading at different temperatures were compared to experimental data from Taheri et al. [11]. As expected, the transformation stresses were accurately predicted. At the same time, the strain seems to be over-estimated with respect to the experimental data. It is thought that the main reason behind these differences could derive from the reduced integration method adopted for the CHEXA element, which could underestimate the element stiffness. As an example, Table 2 compares the theoretical transformation stresses with those obtained from the FEM model at 24 °C.

Table 2. Theoretical vs. FEM analysis transformation stresses at 24 °C.

	Th	FEM	Err%
σ_{M_f} (MPa)	325	314.5	3.2
σ_{M_s} (MPa)	150	147	2.0
σ_{A_f} (MPa)	175	173.8	0.7
σ_{A_f} (MPa)	45	41.4	8.0

2.3.2. Mechanical and Thermal Cycles

To obtain an idea of the SMA rod behaviour, the torque-angle diagram at different temperatures (Figure 13), and the angle-temperature diagram at different torque values (Figure 14), obtained by the FEM analysis, are reported. Note that the angle is measured at the loaded end of the rod.

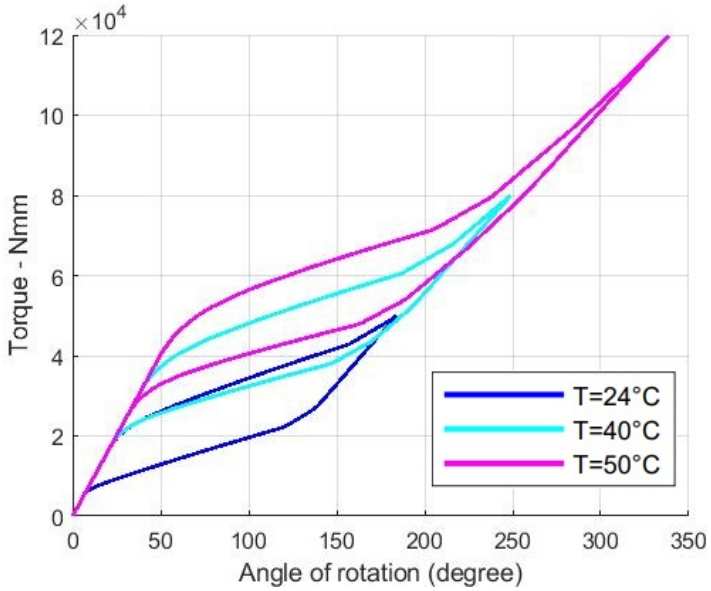

Figure 13. Torque-Angle diagram at 24 °C 40 °C and 50 °C.

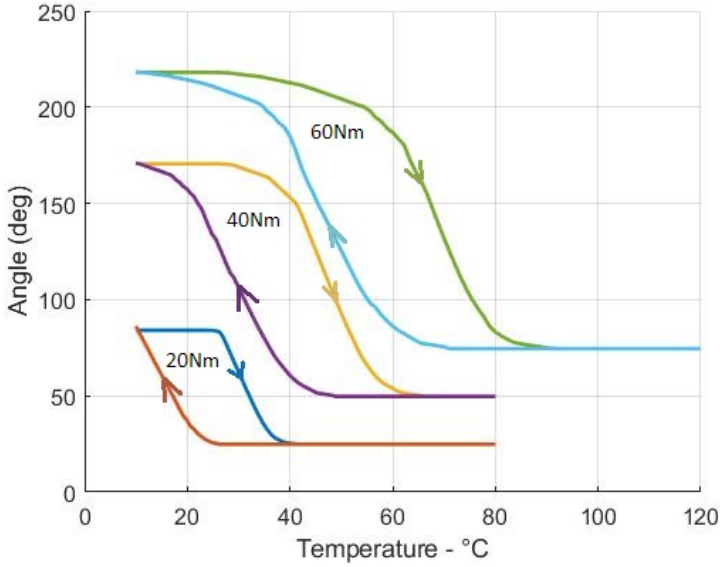

Figure 14. Angle-Temperature diagram under constant torque of 20 Nm, 40 Nm and 60 Nm.

The SMA rod behaviour is thoroughly examined, looking at monitoring stress, temperature, torque and martensite evolution simultaneously, thus providing a holistic vision of the macroscopic phenomena involved in phase transformations. The torque loading cycle is performed, imposing an angular displacement of 180° at 24 °C. For the thermal cycle, the rod is loaded to 40 Nm of torque at 10 °C; subsequently, a complete thermal cycle is obtained, heating the specimen to 80 °C and then cooling it back to 10 °C.

The Martensite volume fraction was considered in the element centroid to avoid physically meaningless results, as in the grid points to higher figures than those that emerged due to data interpolation. Moreover, to reduce border effects, elements in the mid-section along the length of the rod were considered, as shown in Figure 15. The stress was considered in the same points to match the radial position of the two quantities involved in this discussion. A polar diagram of the angular displacement is reported to visualise the rod's motion. Note that the radial value is normalised to one, and does not refer to any physical quantity. Figures 16 and 17 show some snapshots of the mechanical and thermal cycles, respectively.

2.3.3. Actuation with and without Clutch

The specimen considered for the actuation simulation is the same as described in the previous paragraphs. The driven apparatus simulating the return spring and the aerodynamic hinge moment is modelized using a CBUSH element, which is a generalised spring-damper scalar element, associated in this case with the PBUSH and the PBUSHT bulk data entries, to define a load-displacement dependency. Note that the linear load, assumed for simplicity, may be replaced by a generalised loading law acting on the TABLED1 entry. Table 3 summarizes the loading sequence, while Figure 18 shows the torque-angle diagram for the actuator with a clutch. Moreover, Figure 19 highlights the overall behaviour of the SMA under the aforementioned conditions.

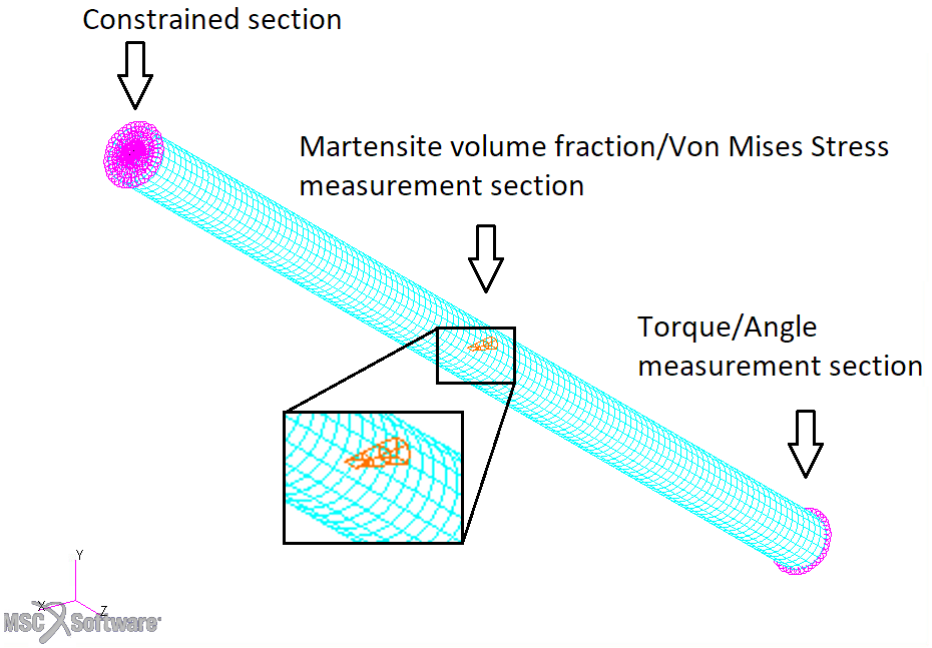

Figure 15. A highlight of relevant sections of the FEM model.

Table 3. Actuator with clutch–Steps sequence.

STEP 0	Set T = 24 °C	
STEP 1	Displacement-driven loading to 172°; T = 24 °C	Blue segment in Figure 18
STEP 2	Unloading to 21 Nm; T = 24 °C	Red segment in Figure 18
STEP 3	Heating 24 °C → 46 °C @ Variable load	Purple segment in Figure 18
STEP 4	Unloading to 21 Nm; T = 46 °C	Green segment in Figure 18
STEP 5	Cooling 46 °C → 0 °C @ Constant load	Cyan segment in Figure 18

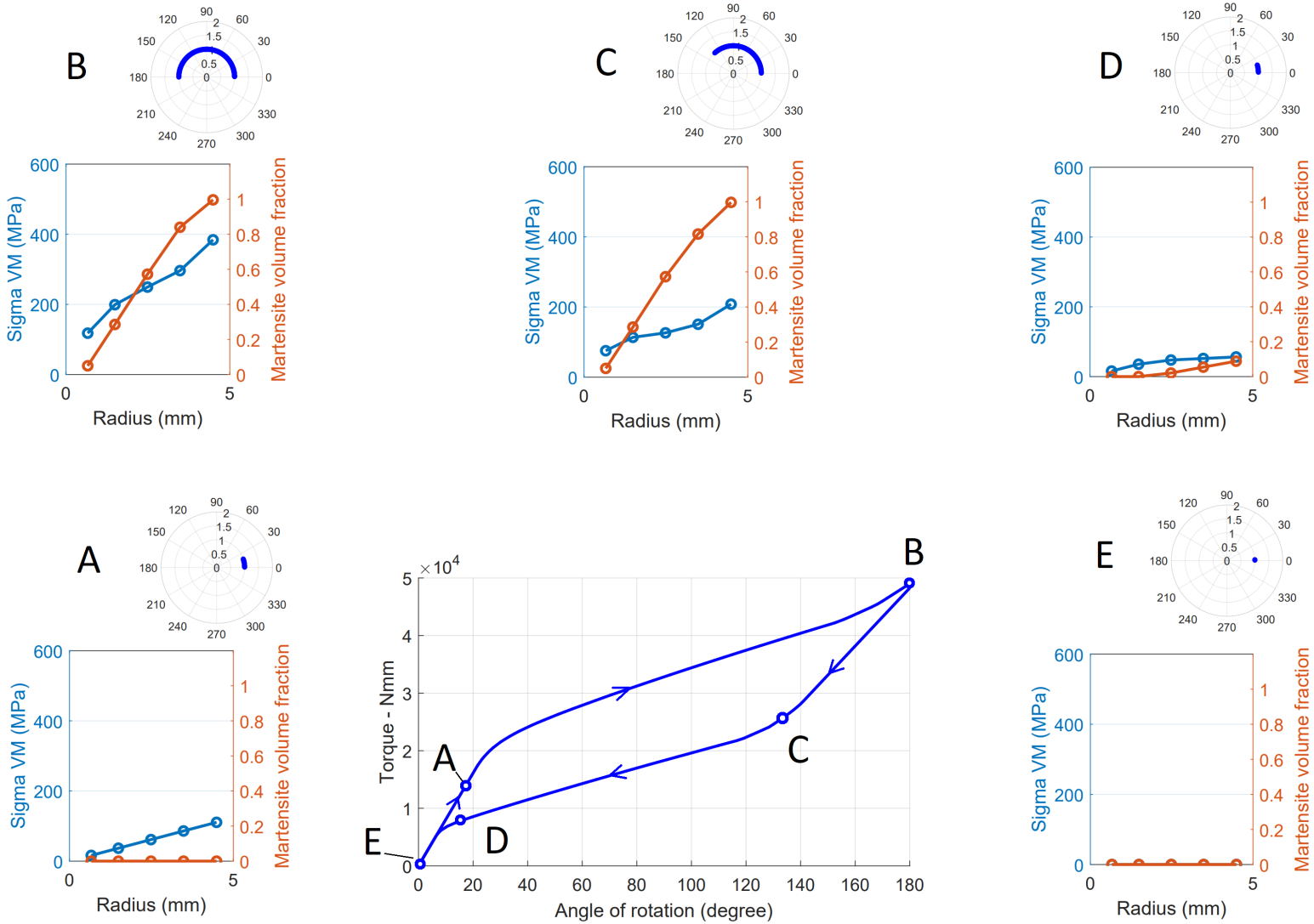

Figure 16. SMA rod behaviour under torque loading cycle @24 °C-FEM model with 5 elements along the radius.

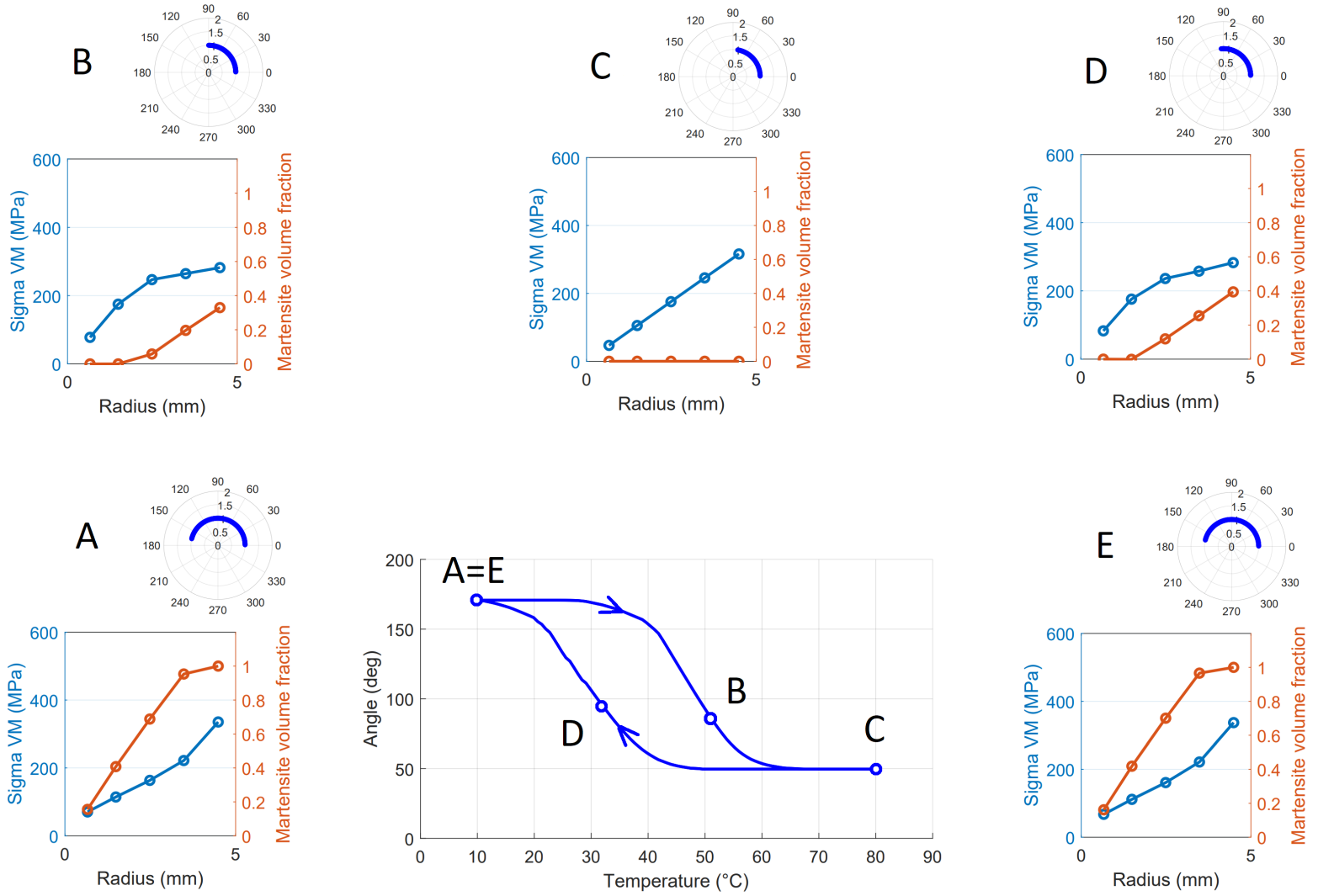

Figure 17. SMA rod behaviour under thermal cycling @40 Nm-FEM model with 5 elements along the radius.

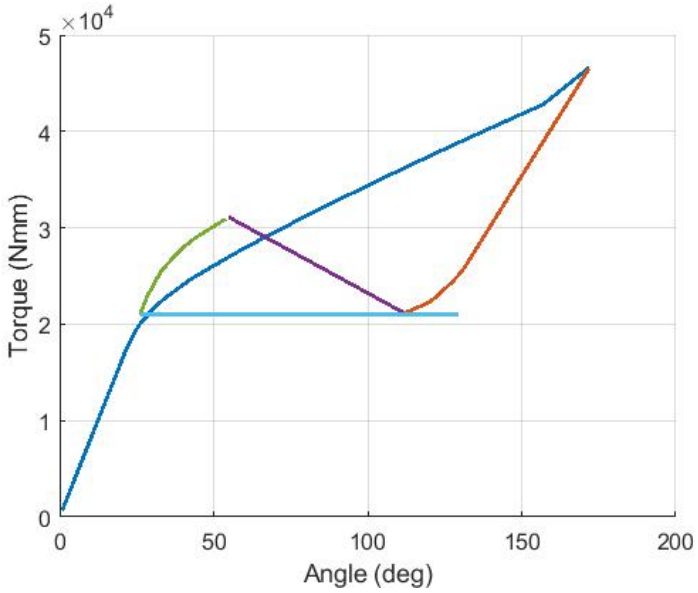

Figure 18. Torque-Angle diagrams—Actuator with clutch.

Concerning the actuator without the clutch, at the end of the forward actuation, the rod is free to return backward (increasing its deformation toward the martensite phase), but cannot move further in the $M \rightarrow A$ transformation direction due to the spline coupling. Note that forward rotations are retained by the locking mechanism acting on the driven shaft at this point. This particular loading condition requires a one-way rotational constraint, which was implemented using an additional CBUSH element described by a strong non-linear law, which is properly engaged using a second MPC. Therefore, as the end of the forward actuation is reached, the one-way constraint was introduced beside a 21-Nm torque. As expected, lowering the temperature under a partial constraint inhibits the austenite-related shape recovery of the rod; however, martensite is still generated. This decreases the effective stiffness of the component and thus reduces the perceived stress. As the rod's resisting torque drops to 21 Nm, the specimen is free to recover its martensitic shape. Interestingly, the generated martensite is the same at the end of the SMA transformations under the same temperature change but different boundary conditions, representing the actuator with and without the clutch. Another fundamental aspect to consider is that Auricchio formulation does not admit twinned martensite. This means that no arguments can be made regarding the formation of twinned martensite under high-temperature and high-stress conditions based on this kind of analysis. The load step sequence is summarised in Table 4, while Figures 20 and 21 show the overall behaviour of the SMA under the aforementioned conditions.

Table 4. Actuator without clutch-Steps sequence.

STEP 0	Set T = 24 °C	
STEP 1	Displacement-driven loading to 172°; T = 24 °C	Blue segment in Figure 20
STEP 2	Unloading to 21 Nm ; T = 24 °C	Red segment in Figure 20
STEP 3	Heating 24 °C → 46 °C @ Variable load	Purple segment in Figure 20
STEP 4	Constant 21 Nm torque; T = 46 °C ; One-way constraint	
STEP 5	Cooling 46 °C → 0 °C @ Constant load with one-way constraint	Cyan segment in Figure 20

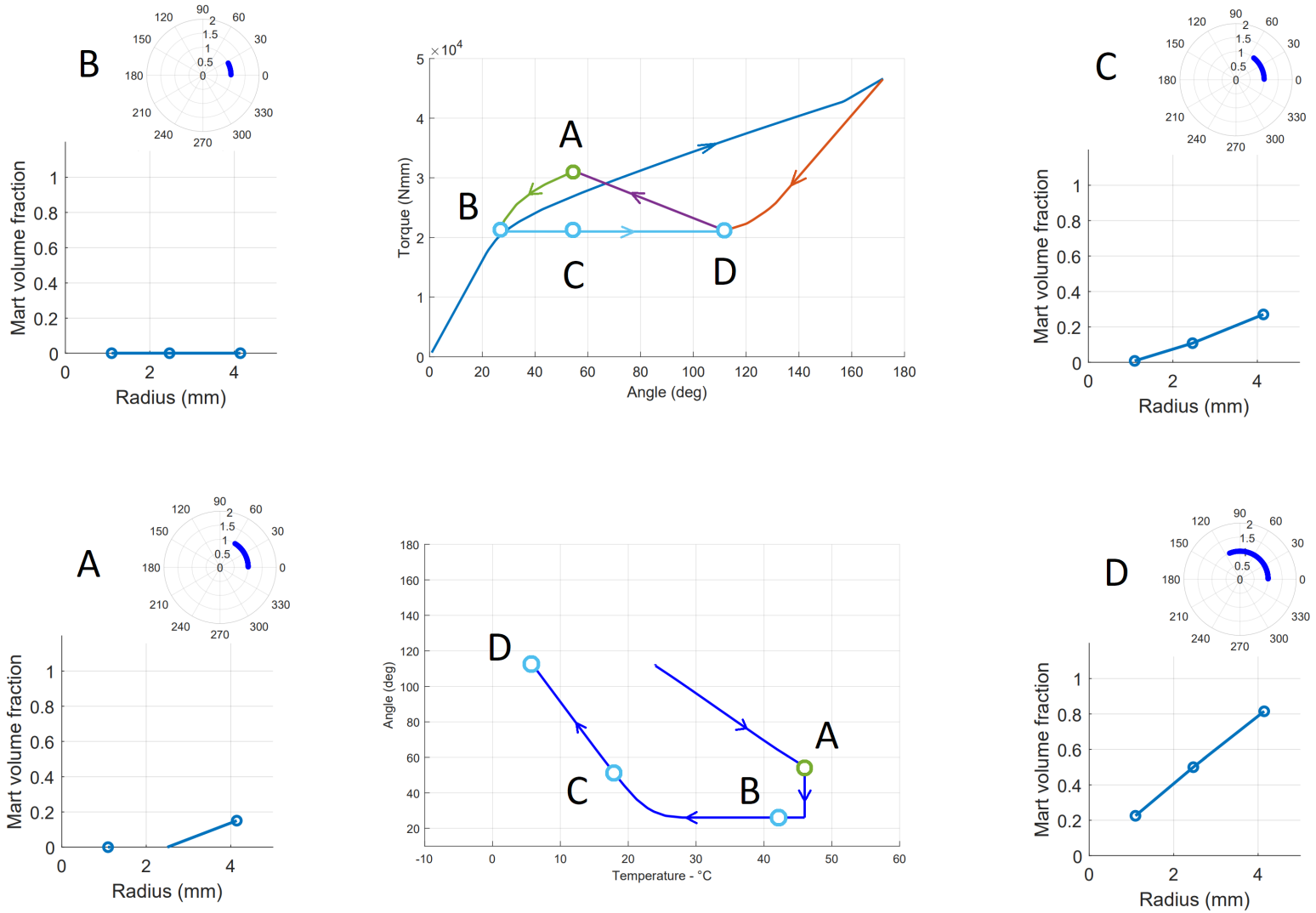

Figure 19. Martensite, displacement, torque and temperature evolution during actuation—Actuator with clutch. FEM model with 3 elements along the radius.

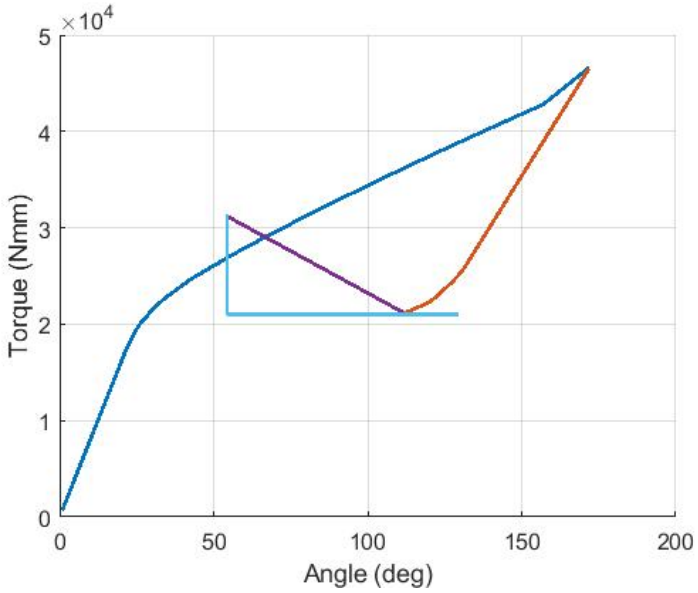

Figure 20. Torque-Angle diagrams—Actuator without clutch.

2.4. Load Estimations

This section aims to estimate the torque involved in the actuation of some secondary control surfaces for three classes of aircraft. The adopted method can be used for a large variety of cases, constituting a helpful tool to obtain approximate values of the needed torque, which is a crucial design specification when developing an actuator. The aircrafts chosen in this work are the medium-size UAV RQ7 Shadow, the Cessna 172 Skyhawk and the ATR 42–600. Indeed, to examine the possibility and implications of scaling-up SMA torsional actuator technology, the aircraft mentioned above belong to three distinct categories. The specific model choice, instead, is based on data availability in the literature and on the web. Indeed most of the required data, presented hereafter, were collected from manufacturer websites, brochures, factsheets and documentation, along with minor details found on other websites. The case study considered here aims to predict the aerodynamic hinge moment applied to the flap during take-off and landing. Moreover, for only the ATR 42, an Adaptive Trailing Edge, as presented in [5], is considered. Take-off and landing speeds were determined based on manufacturer data and certification specification. Referring to the UAV and the four-seats aircraft, EASA CS-23 [19] was adopted, while CS-25 [20] prescriptions were followed in the case of the ATR 42. At this step, considering sea-level standard air condition, it is possible to calculate Reynolds and Mach numbers.

The last unknown to be determined is the hinge moment coefficient, which was found using Xfoil, and its embedded functions "flap" and "hinc". The hinge moment coefficient provided by Xfoil is defined as follows:

$$\frac{HingeMoment}{Span} = C_{HingeMoment}\frac{1}{2}\rho V^2 c^2 \quad (1)$$

where the hinge moment is calculated as a result of the aerodynamic forces with respect to the user-defined hinge location. The analysis was run via a MATLAB script to obtain data at different flight conditions, accounting for several flap angle deflections with respect to the angle of attack. All the data required to determine the hinge moment are summarised in Table 5.

Moreover, as discussed previously, an adaptive trailing edge device for the ATR 42 was assessed. As in [5] a moving surface of 2% of the local chord was assumed. Moreover, a typical cruise condition was considered for regional aircraft. As a compromise between medium- and short-haul flights, an altitude of around 13,000 feet (or 4 km) was selected for this investigation. Given the hinge moment coefficients, the torque, and the data required for their determination under the most demanding conditions, are summarised in Table 6.

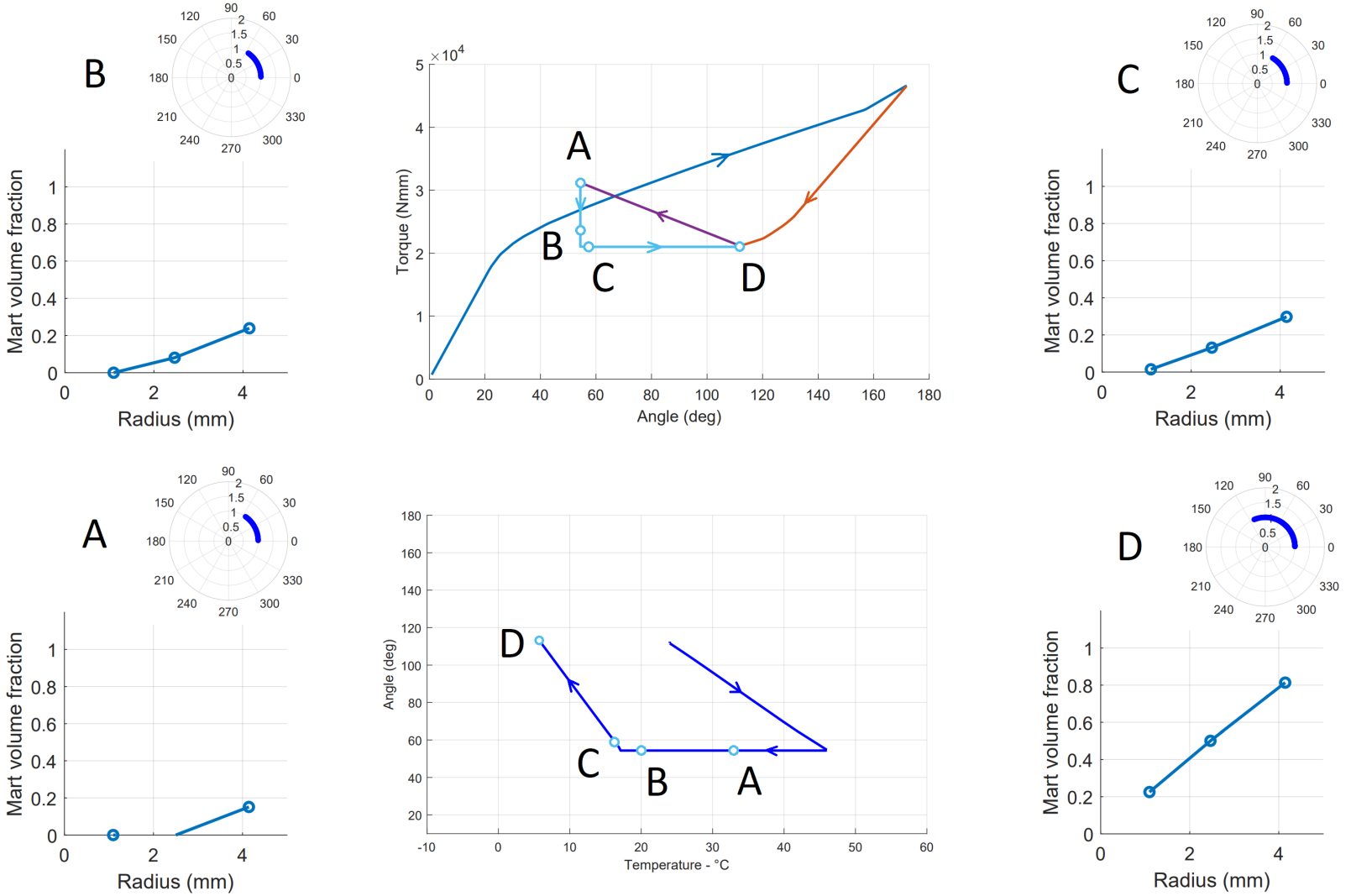

Figure 21. Martensite, displacement, torque and temperature evolution during actuation—Actuator without clutch. FEM model with 3 elements along the radius.

Table 5. Data summary-Flap. (1) Reasonable approximation of the actual airfoil. (2) Hypothetical value.

	RQ7 Shadow			**Cessna 172**			**ATR 42 600**		
Gross weight	170	kg	[21]	1111	kg	[22]	18,600	kg	[23]
Wingspan	3.87	m	[21]	11	m	[22]	24.57	m	[23]
Airfoil	NACA 4415		[21]	NACA 2412		[22]	NACA 23015		(1)
Root chord	0.42	m	[24]	1.63	m	[25]	2.624	m	[23]
Flap chord	0.114	m	[24]	0.491	m	[25]	0.75	m	[23]
Flap span	1.012	m	[24]	2.043	m	[25]	3.498	m	[23]
x_{hinge}%	73%		[24]	70%		[25]	71%		[23]
δ_{max}	40	°	[21]	30	°	[25]	30	°	[23]
Stall speed (V_{s1})	17.5	m/s	(2)	24.2	m/s	[25]	50.99	m/s	
Cruise speed	36	m/s	[21]	62.8	m/s	[22]	154.4	m/s	[23]
Max speed	55.5	m/s	[21]	80	m/s	[22]			
V_2	21	m/s		29	m/s		57	m/s	[23]
V_3	22.75	m/s		31.46	m/s		62.72	m/s	
V_{LND}	34.12	m/s		47.19	m/s		94.08	m/s	
Re_{LND}	9.95×10^5			5.34×10^6			1.71×10^7		
M_{LND}	0.099			0.138			0.274		
V_{TO}	22.75	m/s		31.46	m/s		62.72	m/s	
Re_{TO}	9.19×10^5			4.93×10^6			1.57×10^7		
M_{TO}	0.092			0.127			0.252		
$C_{hinge,max}$	0.34			0.38			0.37		
$M_{hinge,max}$	3.19	Nm		255.28	Nm		3946.69	Nm	
$M_{hinge,max}$/ span	3.15	N		124.95	N		1128.27	N	

In sum, the maximum hinge moment obtained for the RQ7 shadow is about 3.2 Nm, compatible with the torque output of commercially available UAV actuators. The hinge moment calculated for the Cessna 172 is 225 Nm, close to the values achieved by the refined optimisation performed by Florjancic in [26] for the same aircraft (ranging from 332 Nm to 267 Nm). The maximum ATR 42 hinge moment was found to be about 3950 Nm. Although no reference was found to reasonably validate this data, as a means of comparison, a rotary actuator adopted for the motion of the Boeing 777 outboard flap develops a max torque of 12.1 kNm [27]. Finally, a hinge moment of 9.4 Nm was found in the ATE case, which is probably the less accurate result. However, knowing the SMA torque actuator size used in [5] and its related average torque performance, a value of the same magnitude is also expected in this case.

Table 6. Data summary—ATE.

	ATR 42 600	
Airfoil	NACA 23015	
Root chord	2.624	m
Flap chord	0.75	m
Flap span	3.498	m
x_{hinge}%	98%	
δ_{max}	20	°
Cruise speed	154.4	m/s
Re_{cruise}	2.00×10^7	
M_{cruise}	0.467	
$C_{hinge,max}$	0.1	
$M_{hinge,max}$	9.4	Nm
$M_{hinge,max}$/span	2.7	N

3. Concluding Remarks

To obtain a sense of the torque involved in moving control surfaces, aerodynamic load predictions are performed using Xfoil for three classes of aircraft (medium-size UAV, Four-Seat Aircraft and Regional Transport Aircraft), considering a plain flap and an Adaptive Trailing Edge device. The analysis was handled using a Matlab script. The obtained data were compared to those presented in the literature to validate the adopted method.

A general approach based on characteristic curves is provided to conceptually design SMA torsional actuators.

An FEM model is created in MSC Patran and solved by Nastran, which implements Auricchio's formulation. This means provides a holistic vision of the macroscopic phenomena involved during phase transformations, accomplishing either a general method for the preliminary design and a helpful educational tool for those approaching the SMA actuators' design for the first time. Indeed, SMA rods' behaviour under mechanical and thermal loading is thoroughly examined, monitoring stress, temperature, torque and martensite evolution simultaneously.

Operative loading conditions were investigated considering different actuator designs and simulating a full transformation cycle between martensite and austenite. In particular, the specific case of cooling the prestressed SMA, keeping the twist angle constant, was investigated. Two alternative interpretations were found: the first one is based on the assumption of the formation of twinned martensite at high temperatures, while the second one implies the formation of detwinned martensite. In the first case, a decay of the actuation performance is expected, due to the progressive build-up of retained martensite; in the second case, the actuation performance is preserved with cycles, with the transformation martensite remaining constant. This led to a hypothesis regarding the existence of a new region in SMA phase diagrams in which twinned martensite can be found under high-temperature and high-stress conditions. Long-term experimental tests can be performed concerning the cooling effect on constrained austenite specimen from a high-stress and high-temperature state, to dispel any doubt regarding the formation of twinned martensite in these conditions.

The main limit of the proposed FEM model lies in the fact that Auricchio's formulation does not admit twinned martensite. Moreover, no conclusions can be derived from the training effects, since performing a second loading cycle does not present any difference with respect to the first one. Additionally, for the material considered in this dissertation, FEM data overestimate the transformation strain. Experimental data remain mandatory for the final draft and are an indispensable source to understand the governing principles of SMAs.

Finally, it is worth mentioning that the presented model is easily reconfigurable and can be integrated into an optimization loop. Moreover, thermal aspects should be deepened to include the time domain and account for inertial effects, even using non-linear transient solutions.

Author Contributions: All authors conceived the paper and designed the review study. Conceptualization, M.S., S.A., A.C. and E.C.; methodology, M.S., S.A., A.C. and E.C.; software, M.S. and S.A.; validation, M.S., S.A., A.C. and E.C.; formal analysis, M.S.; investigation, M.S.; resources, M.S., S.A., A.C. and E.C.; data curation, M.S.; writing—original draft preparation, M.S.; writing—review and editing, M.S., S.A., A.C. and E.C.; visualization, M.S.; supervision, S.A., A.C. and E.C.; project administration, S.A., A.C. and E.C. All authors have read and agreed to the published version of the manuscript.

Funding: This research received no external funding.

Institutional Review Board Statement: Not applicable.

Informed Consent Statement: Not applicable.

Data Availability Statement: The data presented in this study are available on request from the corresponding author.

Acknowledgments: Special thanks to Mauro Linari for his support in the FEM modelization.

Conflicts of Interest: The authors declare no conflict of interest.

Abbreviations

The following abbreviations are used in this manuscript:

ATE	Adaptive Trailing Edge
FEM	Finite Element Method
SMA	Shape Memory Alloy
UAV	Unmanned Aerial Vehicle

References

1. Calkins, F.T.; Mabe, J.H. Shape memory alloy based morphing aerostructures. *J. Mech. Des.* **2010**, *132*, 111012–111019. [CrossRef]
2. Mabe, J.H.; Calkins, F.T.; Bushnell, G.S.; Bieniawski, S.R. Shape Memory Alloy Actuator. U.S. Patent No 8,118,264, 21 February 2012.
3. Bushnell, G.S.; Arbogast, D.; Ruggeri, R. Shape control of a morphing structure (rotor blade) using a shape memory alloy actuator system. In Proceedings of the SPIE 6928, Active and Passive Smart Structures and Integrated Systems 2008, 69282A, San Diego, CA, USA, 18 April 2008.
4. Arbogast, D.J.; Ruggeri, R.T.; Bussom, R.C. Development of a 1/4-scale NiTinol actuator for reconfigurable structures. In Proceedings of the SPIE 6930, Industrial and Commercial Applications of Smart Structures Technologies 2008, 69300L, San Diego, CA, USA, 19 March 2008.
5. Calkins, F.T.; Mabe, J.H. Flight test of a shape memory alloy actuated adaptive trailing edge flap. In Proceedings of the ASME 2016 Conference on Smart Materials, Adaptive Structures and Intelligent Systems, Volume 1: Multifunctional Materials, Mechanics and Behavior of Active Materials, Integrated System Design and Implementation, Structural Health Monitoring, Stowe, VT, USA, 28–30 September 2016.
6. Stroud, H.; Hartl, D. Shape memory alloy torsional actuators: A review of applications, experimental investigations, modeling, and design. *Smart Mater. Struct.* **2020**, *29*, 113001–113018. [CrossRef]
7. Ameduri, S.; Ciminello, M.; Concilio, A.; Dimino, I.; Galasso, B.; Guida, M. Structural Module for Fixed and Rotary Wing. EP Patent Application No. 21425028, 25 May 2021.
8. Auricchio, F.; Bonetti, E.; Scalet, G.; Ubertini, F. Theoretical and numerical modeling of shape memory alloys accounting for multiple phase transformations and martensite reorientation. *Int. J. Plast.* **2014**, *59*, 30–54. [CrossRef]
9. Popov, P.; Lagoudas, D.C. A 3-D constitutive model for shape memory alloys incorporating pseudoelasticity and detwinning of self-accommodated martensite. *Int. J. Plast.* **2007**, *23*, 1679–1720 . [CrossRef]
10. Mirzaeifar, R.; DesRoches, R.; Yavari, A. Exact solutions for pure torsion of shape memory alloy circular bars. *Mech. Mater.* **2010**, *42*, 797–806. [CrossRef]
11. Taheri Andani, M.; Alipour, A.; Eshghinejad, A.; Elahinia, M. Modifying the torque–angle behavior of rotary shape memory alloy actuators through axial loading: A semi-analytical study of combined tension–torsion behavior. *J. Intell. Mater. Syst. Struct.* **2013**, *24*, 1524–1535. [CrossRef]
12. Benafan, O.; Gaydosh, D.J. High Temperature Shape Memory Alloy Ni50.3Ti29.7Hf20 Torque Tube Actuators. *Smart Mater. Struct.* **2017**, *26*, 95002–95011. [CrossRef]
13. Mabe, J.; Ruggeri, R.; Rosenzweig, E.; Yu, C. NiTinol Performance Characterization and Rotary Actuator Design. In Proceedings of the SPIE 5388, Smart Structures and Materials 2004: Industrial and Commercial Applications of Smart Structures Technologies, San Diego, CA, USA, 29 July 2004.
14. Pecora, R.; Ameduri, S.; Rea, F. Active Metal Structures. In *Morphing Wing Technologies: Large Commercial Aircraft and Civil Helicopters*; Ricci, S., Dimino, I., Lecce, L., Pecora, R., Aliabadi Ferri, M.H., Botez, R., Semperlotti, F., Eds.; Butterworth-Heinemann: Oxford, UK, 2018; pp. 302–311.
15. Auricchio, F. A robust integration-algorithm for a finite-strain shape-memory alloy superelastic model. *Int. J. Plast.* **2001**, *17*, 971–990. [CrossRef]
16. Auricchio, F.; Taylor, R. Shape-memory alloys: Modelling and numerical simulations of the finite-strain superelastic behavior. *Comput. Methods Appl. Mech. Eng.* **1997**, *143*, 175–194. [CrossRef]
17. *MSC Nastran 2013.1.1-Quick Reference Guide*; MSC SOFTWARE, Siemens Industry Software Headquarters Granite Park One 5800 Granite Parkway Suite 600: Plano, TX, USA, 2013; pp. 2700–2073.
18. *MSC Nastran 2021 Nonlinear (SOL 400)-User's Guide*; MSC SOFTWARE, Siemens Industry Software Headquarters Granite Park One 5800 Granite Parkway Suite 600: Plano, TX, USA, 2021; pp. 599–602.
19. *Certification Specifications for Normal, Utility, Aerobatic, and Commuter Category Aeroplanes CS-23*; EASA Amendment 3, EASA Headquarter Konrad-Adenauer-Ufer 3: Cologne, Germany, 2012; pp. 1B2–1B10.
20. *Certification Specifications for Large Aeroplanes CS-25*; EASA, Amendment 3, EASA Headquarter Konrad-Adenauer-Ufer 3: Cologne, Germany 2007; pp. 1B3–1B12.

21. AAI RQ-7 Shadow-Specifications (200 Family). Available online: https://en.wikipedia.org/wiki/AAI_RQ-7_Shadow (accessed on 8 May 2021).
22. Cessna 172. Available online: https://en.wikipedia.org/wiki/Cessna_172 (accessed on 8 May 2021).
23. ATR 42-600. Available online: https://www.atr-aircraft.com/our-aircraft/atr-42-600/ (accessed on 8 May 2021).
24. AAI RQ-7B Shadow 200 Technical Sketch. Available online: https://aviationsmilitaires.net/v3/kb/picture/7236/aai-rq-7b-shadow-200 (accessed on 8 May 2021).
25. Skyhawk Model 172S-Specification & Description. Available online: https://www.aeromecanic.com/Skyhawk_DOC_FR_files/spec.pdf (accessed on 8 May 2021).
26. Florjancic, D. Improved Design of a High Lift System for General Aviation Aircraft. Master Thesis, TU Delft, Delft, The Netherlands, 25 August 2015.
27. Zaccai, D.; Bertels, F.; Vos, R. Design methodology for trailing-edge high-lift mechanisms. *CEAS Aeronaut. J.* **2016**, *7*, 521–534. [CrossRef]